

See discussions, stats, and author profiles for this publication at: <https://www.researchgate.net/publication/232322800>

Preparation and Tribological Study of Functionalized Graphene \AA IL Nanocomposite Ultrathin Lubrication Films on Si Substrates

ARTICLE in THE JOURNAL OF PHYSICAL CHEMISTRY C · JUNE 2011

Impact Factor: 4.77 · DOI: 10.1021/jp111804a

CITATIONS

33

READS

105

7 AUTHORS, INCLUDING:



Pu Jibin

Chinese Academy of Sciences

34 PUBLICATIONS 302 CITATIONS

[SEE PROFILE](#)



Shanhong Wan

Lanzhou Railway Institute

25 PUBLICATIONS 224 CITATIONS

[SEE PROFILE](#)



Wenjie Zhao

Chinese Academy of Sciences

37 PUBLICATIONS 380 CITATIONS

[SEE PROFILE](#)



Yufei Mo

Guangxi University

32 PUBLICATIONS 453 CITATIONS

[SEE PROFILE](#)

Preparation and Tribological Study of Functionalized Graphene–IL Nanocomposite Ultrathin Lubrication Films on Si Substrates

Jibin Pu,^{†,‡} Shanhong Wan,[†] Wenjie Zhao,[§] Yufei Mo,^{||} Xiaoqian Zhang,[†] Liping Wang,^{*,†} and Qunji Xue[†]

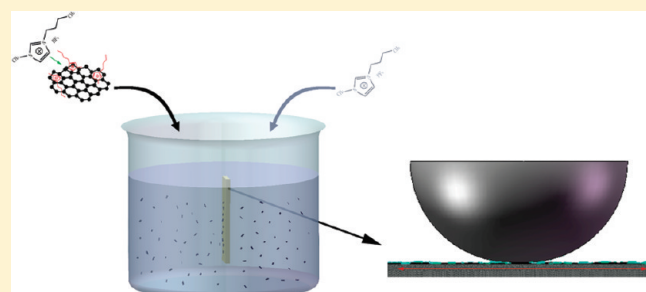
[†]State Key Laboratory of Solid Lubrication, Lanzhou Institute of Chemical Physics, Chinese Academy of Science, Lanzhou 730000, China

[‡]Graduate School of Chinese Academy of Science, Beijing 100080, China

[§]Ningbo Institute of Material Technology & Engineering, Chinese Academy of Sciences

^{||}School of Chemistry & Chemical Engineering, Guangxi University, Nanning 530004, P. R. China

ABSTRACT: Nanocomposite materials based on graphene and ionic liquids (ILs) with unique and highly attractive properties have received considerable interest in various research fields, including biosensors, electrochemical sensors, and so on. Given the excellent mechanical properties and frictional properties of graphene nanosheets, nanocomposite ultrathin films composed of graphene nanosheets and ionic liquids (ILs) with excellent lubricating property are expected to possess improved comprehensive tribological performance. In the current paper, various functionalized graphene–IL nanocomposite ultrathin lubrication films on Si substrates, on the basis of the good dispersion of graphene nanosheets that were noncovalently functionalized by imidazolium-based ILs in acetone, were successfully prepared by an electrostatic adsorption method and were confirmed by several characterization techniques. Appropriate amounts of functionalized graphene nanosheets uniformly distributed on the substrate surface without overlapping greatly enhanced the load-carrying capacity of the ultrathin lubrication films, and the new nanocomposite films gave excellent micro/nanotribological properties. The novel nanocomposite films are hoped to find promising applications in the lubrication of micro/nanoelectromechanical systems (MEMS/NEMS).



INTRODUCTION

Because of its excellent mechanical properties,¹ novel physical properties, and large theoretical specific surface area,² graphene, a flat monolayer of carbon atoms tightly packed into a honeycomb two-dimensional lattice,³ has received considerable interest for its potential applications in many technological fields, such as nanoelectronics,⁴ sensors,⁵ nanocomposites,⁶ batteries,⁷ supercapacitors,⁸ and the like. Graphene is the building block of the most common macroscopic solid lubricant, graphite, which exhibits low friction and wear rates.³ Therefore, besides its excellent electronic and mechanical properties, the lubricating property of graphene is also of interest for application in future micro/nanoelectromechanical systems (MEMS/NEMS). Thus far, both experimental and theoretical results of the nanoscale friction of a graphene sheet as determined by atomic force microscopy (AFM) have been reported.⁹ Filleter et al.¹⁰ suggested that graphene films could be used to further reduce friction on silicon carbide surfaces, which are already technologically used as low-friction antiwear coatings, and found that such films exhibit frictional properties rather similar to those of bulk graphite. A reduction in friction attributed to graphene layers and a variation in friction between graphene layers of different thicknesses have also been found on silicon oxide surfaces.¹¹ Investigation results from Ou et al.¹² have shown that reduced graphene oxide (RGO)

covalently assembled onto a silicon surface exhibits excellent friction reduction and wear resistance properties under a low applied load. Considerable efforts have recently been made to fabricate different graphene-based nanocomposites and to explore their applications in various fields⁶ thus motivating investigations of graphene-based nanocomposite lubrication films.

Room-temperature ILs (RTILs), broadly defined as salts composed of bulky organic cations and smaller anions that exist in the liquid state at room temperature,¹³ have found wide applications in many fields owing to their negligible volatility,¹⁴ high ionic and thermal conductivity, nonflammability, controlled miscibility with a large variety of organic and inorganic compounds, and designable properties¹⁵ among others. These unique characteristics of RTILs also exactly fit the demands of high-performance lubricants.¹⁶ Extensive research has shown that RTILs possess excellent lubrication performance as both lubrication oils and additives.¹⁷ Many groups have recently paid considerable attention to the desirable micro/nanotribological properties of RTILs as ultrathin films several nanometers thick on polished silicon or diamondlike carbon (DLC) surfaces as potential molecular-level lubricants for reducing friction in

Received: December 12, 2010

Revised: March 26, 2011

Published: June 21, 2011

MEMS/NEMS.¹⁸ However, the insufficient antiwear performance of pure RTIL ultrathin films has restricted their applications in MEMS/NEMS. To further enhance the load-carrying capacity and the antiwear properties of ultrathin RTIL films, investigations on two-phase RTIL films with both reducing friction and load-carrying phases have been carried out.¹⁹ In view of the above-mentioned mechanical strength and the low friction of graphene, it is therefore quite interesting to investigate the effect of graphene as a load-carrying phase on the tribological behavior of RTIL-based nanocomposite lubrication films. However, the dispersion of graphene nanosheets in ultrathin RTIL films has remained a great challenge to researchers in the pursuit of determining the synergistic effects of solid graphene and liquid RTILs.

Several methods for preparing graphene are available, such as repeated mechanical cleavage,²⁰ chemical exfoliation,²¹ thermal exfoliation,²² chemical vapor decomposition,²³ and so on. The reduction of exfoliated graphite oxide from its colloidal suspensions has proven to be an effective and reliable method of producing graphene on a large scale.²⁴ However, while hydrophilic graphene oxide (GO) could readily be dispersed in water via the electrostatic repulsion of negatively charged oxygen groups on GO surfaces, the RGO obtained through chemical conversion tends to form irreversible agglomerates through strong $\pi-\pi$ stacking and van der Waals interactions²⁵ making further processing and manipulation difficult. In this regard, several techniques, including noncovalent and covalent functionalizations of RGO with organic molecules, have been developed to prevent the irreversible aggregation of RGO during chemical reduction.²⁶ Some groups recently employed ILs as graphene stabilizers because of their wide solubility and surface-charge introduction²⁷ thus providing new opportunities to investigate well-dispersed graphene nanosheets noncovalently functionalized with hydrophilic imidazolium-based RTILs by cation- π or $\pi-\pi$ interactions.

In the present work, hydrophilic 1-butyl-3-methylimidazolium tetrafluoroborate ([BMIM][BF₄]) and hydrophobic 1-butyl-3-methylimidazolium hexafluorophosphate ([BMIM][PF₆]), both of which have excellent lubrication performance, are separately selected as a stabilizer and lubricant, respectively, of nanocomposite films. The reduced GO nanosheets noncovalently functionalized (f-RGO) with hydrophilic [BMIM][BF₄] are first dispersed in a dilute solution of [BMIM][PF₆] in acetone via electrostatic repulsions. The introduction of [BMIM][BF₄] on the RGO surface not only increases the dispersion of graphene nanosheets in acetone but also provides surface charges for further electrostatic adsorption of RGO on hydroxylated Si surfaces. A nanocomposite ultrathin lubrication film that combines lubricating [BMIM][PF₆] and antiwear f-RGO is successfully prepared on a Si substrate using an electrostatic adsorption method. The micro/nanotribological performances of the as-prepared functionalized graphene-IL nanocomposite ultrathin lubrication films are reported with the aim of acquiring insights into their potential in resolving the tribological problems of MEMS/NEMS. Furthermore, the effects of f-RGO density in dispersion of functionalized graphene-ILs on the tribological properties of the resultant nanocomposite films are also extensively investigated.

■ EXPERIMENTAL SECTION

Materials. [BMIM][PF₆] and [BMIM][BF₄] ILs were synthesized and purified. Graphite powders (purchased from Qingdao Hensen Graphite Co., China) were used for the preparation of GO.

P-type polished single-crystal Si(100) wafers (obtained from GRINM Semiconductor Materials Co., Beijing, China) were used as substrates. All other reagents were of analytical grade and were used as received. Deionized water was used for the preparation of all aqueous solutions and for rinsing.

Preparation of GO Dispersion. GO was synthesized from graphite powders by a modified Hummers and Offeman method.²⁸ Briefly, the preoxidized graphite powders (1 g) were added to concentrated H₂SO₄ (23 mL) in an ice bath. KMnO₄ (3 g) was then slowly added to the mixture with stirring so that the mixture remained below 20 °C. After thorough dispersal, the mixture was stirred at 35 °C for 30 min. Deionized water (46 mL) was gradually added, and the mixture was allowed to stand for 15 min without stirring. The mixture was then further diluted with deionized water (140 mL) and was treated with 30% H₂O₂ (12.5 mL). The resulting mixture was filtered and was washed with 10% aq HCl (200 mL) to remove metal ions followed by dialysis and repeated washing with deionized water until the pH of the filtrate was neutral. Finally, a diluted, homogeneous, yellow-brown GO dispersion was obtained by ultrasonication and centrifugation.

Preparation of Acetone Dispersions of Functionalized Graphene-ILs. A brief preparation process of the dispersion is as follows: An aqueous solution of [BMIM][BF₄] (25 mL, 10 mg·mL⁻¹) was mixed with the aqueous GO dispersion (25 mL, 1 mg·mL⁻¹) with the aid of ultrasonication. The homogeneous GO dispersion was then reduced by 85% hydrazine hydrate (17 mL) at 95 °C for 2 h under reflux. After chemical reduction, the resulting suspension was subjected to ultrasonication, dialysis, and washing in sequence. The resulting stable aqueous dispersion of reduced GO noncovalently functionalized (f-RGO) with [BMIM][BF₄] was then centrifuged to remove excess ILs. Finally, three kinds of dispersions of functionalized graphene-ILs in acetone (0.2/2, 0.1/2, and 0.01 mg·mL⁻¹/2 mg·mL⁻¹) were obtained by mixing different amounts of [BMIM][BF₄]-stabilized f-RGO and [BMIM][PF₆] acetone solutions with ultrasonication.

Preparation of Nanocomposite Films. The 10 × 10 × 0.5 mm³ Si wafers were ultrasonicated in acetone followed by ethanol for 10 min and then were hydroxylated in freshly prepared Piranha solution, which was composed of a mixture of 7:3 (v/v) 98% H₂SO₄ and 30% H₂O₂ at 90 °C for 30 min. The piranha-treated Si wafers were copiously rinsed with deionized water and were dried in a N₂ stream. These hydroxylated Si wafers were then dipped into the three acetone dispersions of functionalized graphene-ILs for 3 min and were withdrawn from the solutions at a constant velocity of 60 μm/s to allow the formation of targeted lubrication films with approximately 5 nm thickness. The corresponding nanocomposite films were labeled as (0.2)f-RGO/ILs, (0.1)f-RGO/ILs, and (0.01)f-RGO/ILs. For comparison, a sample denoted as pure ILs was prepared from pure [BMIM][PF₆] solution (2 mg·mL⁻¹) using the same procedure. Finally, the films were heated in N₂ at 120 °C for 30 min to successfully produce the desired ultrathin lubrication films on the Si surfaces. All procedures were carried out in a class-100 clean room at 20 °C and a humidity of 18%.

Characterization of the GO, f-RGO, and Lubrication Films. The GO and f-RGO were characterized using field-emission scanning electron microscopy (FE-SEM, JSM-6701F, Hitachi), high-resolution transmission electron microscopy (HRTEM, JEM-2010), multimode atomic force microscopy (AFM, Nanoscope IIIa,

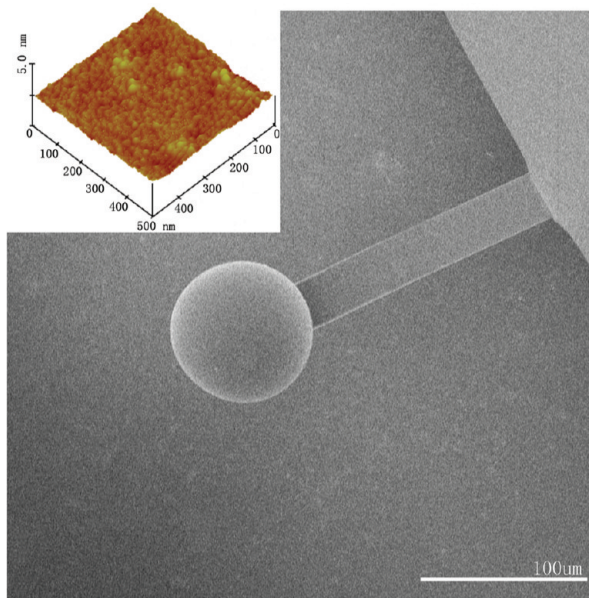


Figure 1. SEM image of the colloid probe and AFM topography of microsphere.

Veeco, tapping mode), Fourier transform infrared spectroscopy (FTIR, IFS 66 V/S, Bruker), X-ray photoelectron spectroscopy (XPS, PHI-5702, Physical Electronics, Al K α irradiation), Raman spectroscopy (Lab JY-HR800, Horiba, with 532 nm laser excitation), and Zetaplus analysis (Malvern, Nano ZS ZEN 3600). XPS and AFM were also used for the characterization of the lubrication films. The binding energies were referenced to the C 1s line at 284.8 eV. The thickness measurements were performed on an L116E ellipsometer equipped with a He–Ne laser set (632.8 nm) at an incident angle of 50° (Gaertner, United States). Averages were obtained from 10 measurement locations on each sample. The static water contact angles were determined using a DSA100 contact angle meter (Krüss, Germany). The water droplet volume used for the measurement was about 5 μ L.

Tribological Properties of the Lubrication Films. AFM is widely used in nanotribological and adhesion measurements in addition to surface morphology characterization. In the current study, the nanofriction of the lubrication films were measured using a homemade colloidal probe mounted on the same AFM in contact mode. The colloidal probe (normal force constant of 2 N m $^{-1}$) was prepared by gluing a microsphere with a radius of 28 μ m onto a tipless cantilever. An FE-SEM image of the colloidal probe and the AFM topography of the microsphere are shown in Figure 1. When the microsphere slid at a scan rate of 1 Hz over a 60 μ m scan line, the voltage signals of the lateral torsion of the cantilever were continuously measured as a function of linearly increasing external loads (\sim 270 nN). The nanofriction forces were then further quantified by determining the lateral spring and lateral detector sensitivity according to Vakarelski et al.'s method.²⁹ Each presented curve represents an average of three different measurements. The same colloidal probe was used to obtain the adhesive behaviors of the lubrication films. The pull-off force was assumed as the adhesive force, which was given by $F_{\text{adhesion}} = K_c Z_p$,³⁰ where K_c is the normal force constant of the colloidal probe and Z_p is the vertical displacement of the piezotube, that is, the deflection of the colloidal probe. The average of 10 individual measurements was obtained for each sample. Before each test,

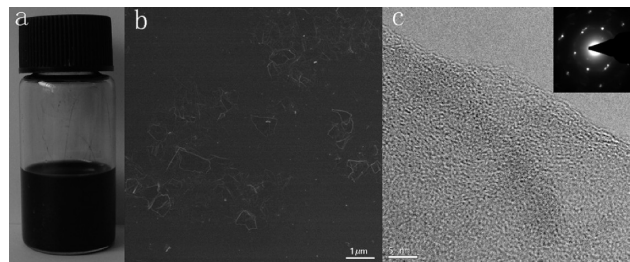


Figure 2. (a) Optical image of the stable aqueous dispersion (0.2 mg mL $^{-1}$) of f-RGO; (b) FE-SEM image of f-RGO deposited on Si surface by drop-casting dilute aqueous dispersion of f-RGO; (c) HRTEM image of f-RGO. The inset is the SAED pattern.

prescanning of the colloidal probe was carried out on a cleaved mica surface to remove physically adsorbed lubricants. All experiments were carried out at 22 °C with a relative humidity of 25%.

Microtribological tests were carried out on an UMT-2MT tribometer (CETR, United States) in the ball-on-plate reciprocating mode. Commercially available steel balls with a diameter of 3.18 mm were used as the stationary upper counterparts, while the lower specimens were adhered onto a reciprocating table with a traveling distance of 5 mm. The friction coefficient versus sliding time curves were recorded automatically in real time, and at least three repeated measurements for each test condition were performed. A failure of the lubrication film is assumed to occur when the friction coefficient rises sharply to a high and stable value similar to that of a clean silicon oxide against the same counterpart (about 0.65); the sliding time was recorded as the antiwear life of the lubrication film. The wear scar morphologies of the lubrication films were observed using a MicroXAM 3D noncontact interferometric microscope with a phase mode (ADE, United States). All tests were conducted at 20 °C and at a relative humidity of 22%.

RESULTS AND DISCUSSION

Figure 2a shows the photograph of stable and dark f-RGO aqueous dispersions. [BMIM][BF₄]⁻, which is attached on the surface of the RGO by noncovalent cation–π or π–π interactions between the imidazolium rings and RGO,^{27,31} causes RGO to attain a positive charge; thus, the resulting electrostatic repulsion among the f-RGO prevented f-RGO aggregation during chemical reduction thereby greatly enhancing their dispersion in the aqueous solution. Moreover, the introduction of the freely soluble [BMIM][BF₄]⁻ to the RGO surface also increased the dispersion of RGO in acetone, which was convenient for the fabrication of the nanocomposite films by electrostatic adsorption. The zeta potentials (ζ) of the GO and f-RGO aqueous dispersions were measured to ensure that the GO was successfully modified with [BMIM][BF₄]⁻. The GO zeta potential value was found to be -38 mV (pH = 6 prepared by thoroughly rinsing with high-purity water until the pH was close to neutral); this was apparently a result of the ionization of GO carboxylic acid and phenolic hydroxyl groups. The zeta potential of f-RGO dramatically changed to +25 mV. The charge reversal, from negative to positive, indicates [BMIM][BF₄]⁻ adsorption on the f-RGO surface. From the FE-SEM image of f-RGO shown in Figure 2b, a small number of overlapping flakelike f-RGO with lateral sizes ranging from a few hundred nanometers to about one

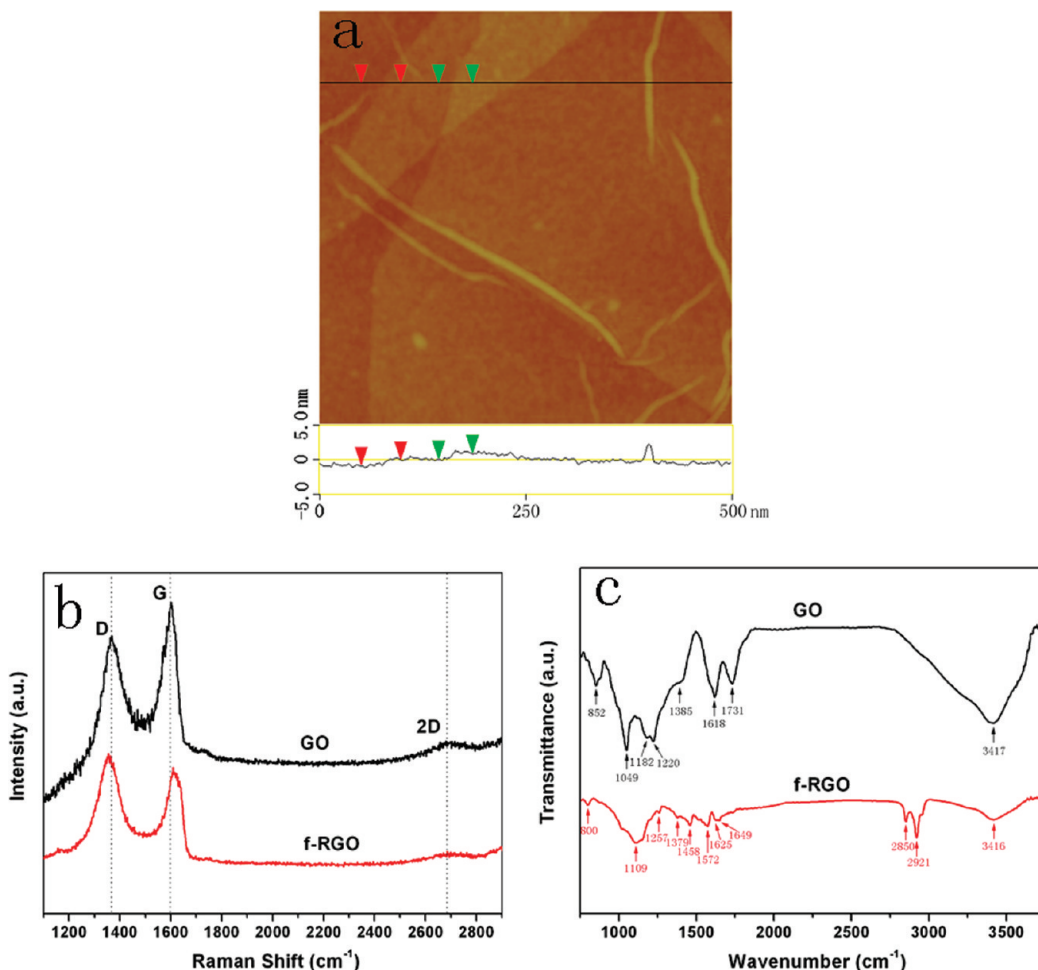


Figure 3. (a) Tapping-mode AFM height image of occasional monolayer f-RGO deposited on freshly cleaved mica surface by drop-casting dilute aqueous dispersion of f-RGO; (b) Raman spectra of GO and f-RGO; (c) FTIR spectra of GO and f-RGO.

micrometer were found on the Si surface. Figure 2c shows a typical HRTEM image of f-RGO; the as-prepared f-RGO was relatively smooth with sharp edges and ripples similar to previous reports.³² Generally, the graphene layers can be distinguished by their folded edges.³³ On the basis of our HRTEM observations, the f-RGO was predominantly the few-layer graphene with three to five layers. The selected area electron diffraction (SAED) pattern of the few-layer f-RGO, as shown in the inset in Figure 2c, showed a clear six-fold pattern revealing the graphitic crystalline nature of the f-RGO.³⁴

AFM was used to characterize the occasional monolayer f-RGO deposited on the freshly cleaved mica surface by drop-casting dilute f-RGO aqueous dispersions and by drying them at ambient temperature (Figure 3a). The f-RGO with different lateral dimensions appeared to overlap, which is a consequence of the sample deposition process; some thicker wrinkled regions were also presented on f-RGO. The average thickness of the monolayer f-RGO was around 0.9 nm from the corresponding cross-sectional view. This thickness is larger than the theoretical value for pristine graphene (i.e., 0.34 nm) but is a typical characteristic of monolayer graphenes modified by alkyl-substituted imidazolium-based ILs taking into account the overestimation in the AFM measurements.²⁷ The increased thickness indicates the existence of [BMIM][BF₄] molecules across the exfoliated RGO surface.

Figure 3b shows the Raman spectra of the GO and f-RGO. GO displayed two prominent peaks, namely, the G band at 1600 cm^{-1} corresponding to the in-plane vibration of the sp²-bonded carbon in a hexagonal lattice and the D band at 1368 cm^{-1} , which is associated with the vibration of the disordered sp³-hybridized carbon because of in-plane defects.³⁵ After noncovalent functionalization with [BMIM][BF₄], the f-RGO G band was broadened and shifted to 1608 cm^{-1} , whereas the D band became significantly stronger than GO. The G band broadening and blue-shifting reflects the disordered and improved exfoliation of the graphene layers.³⁶ The ratio of the D and G band intensities is often used as an indication of the level of chemical modification in a graphitic carbon sample. The Raman spectrum of the f-RGO showed an increased I_D/I_G ratio compared with GO indicating a decrease in the size of the in-plane sp² domains and an increase in the number of sp³ carbons after functionalization.^{21,37} The intensity of the 2D band originating from the two-phonon double-resonance process was weak and broad because of the disorder of the graphene layers, and the broad 2D peak caused difficulties in the exact identification of the number of layers present. We suggested that this feature is dominated by edge effects, as the Raman excitation beam spot size of $\sim 1.5\ \mu\text{m}$ is larger than most of the graphene nanosheets, and the possibility that some of the graphene was reaggregated during sample preparation cannot be ruled out. Nevertheless, the

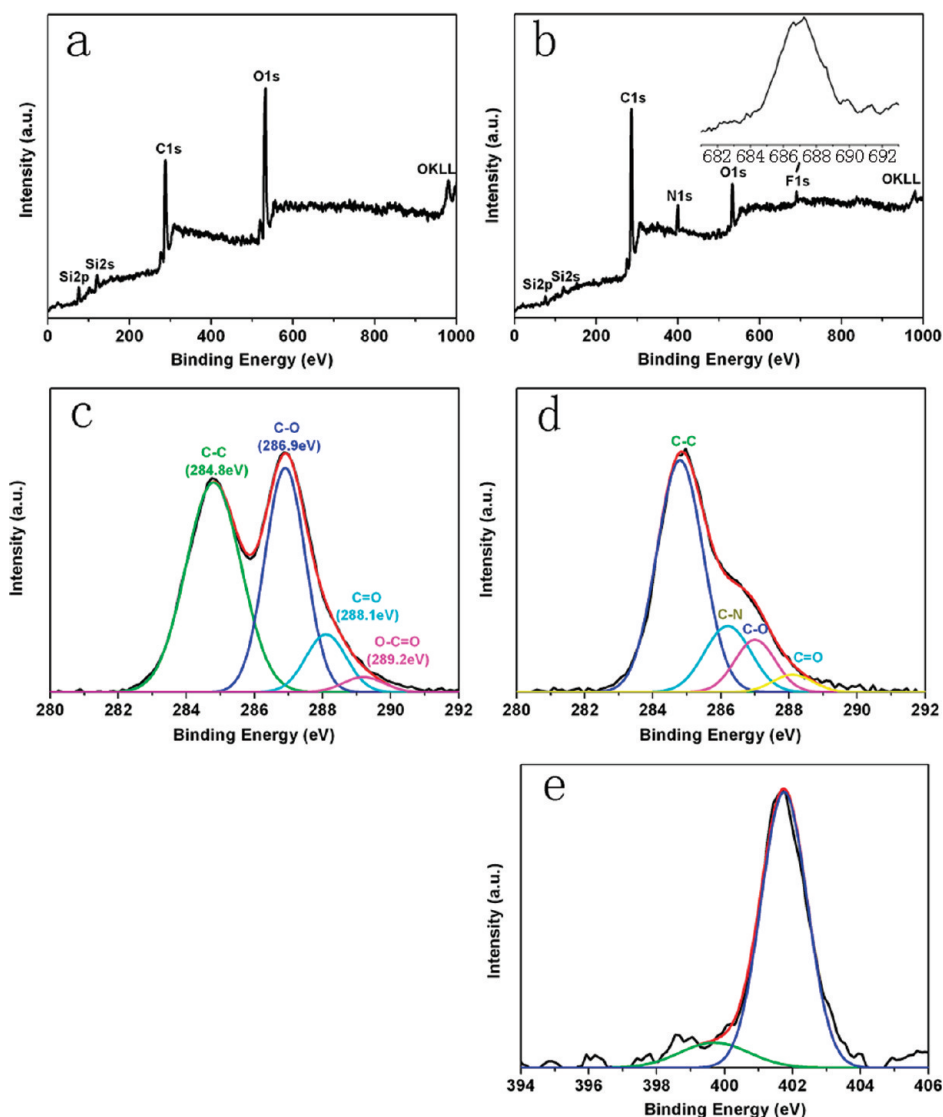


Figure 4. XPS survey spectra of (a) GO and (b) f-RGO; deconvoluted C 1s XPS spectra of (c) GO and (d) f-RGO; (e) deconvoluted N 1s XPS spectrum of f-RGO. The inset in b is F 1s XPS spectrum.

shape and position of the 2D band identified the f-RGO as graphene nanosheets with few layers.³⁸ The FTIR spectra in Figure 3c give the characteristic absorption of the GO and f-RGO functional groups. The FTIR spectrum of GO showed alkoxy/alkoxide ν_{OH} at 3417 cm^{-1} , carboxylic $\nu_{\text{C=O}}$ at 1731 cm^{-1} , aromatic $\nu_{\text{C=C}}$ at 1618 cm^{-1} , alkoxy/alkoxide δ_{OH} at 1385 cm^{-1} , epoxide/ether $\nu_{\text{C-O}}$ at 1220 cm^{-1} and 1182 cm^{-1} , alkoxy/alkoxide $\nu_{\text{C-O}}$ at 1049 cm^{-1} , and epoxide $\nu_{\text{C-O}}$ at 852 cm^{-1} . Compared with GO, the FTIR spectrum of f-RGO showed a decrease in the C=O and C-O stretch intensities confirming its deoxygenation after chemical reduction. Moreover, aside from the remnant δ_{OH} (3416 cm^{-1}) and $\nu_{\text{C-O}}$ (1109 cm^{-1}) and restored aromatic $\nu_{\text{C=C}}$ (1625 and 1649 cm^{-1}), additional methylene symmetric ν_{CH} (2850 cm^{-1}) and asymmetric ν_{CH} (2921 cm^{-1}) as well as $\nu_{\text{C-N}}$ (1572 and 1257 cm^{-1}) and δ_{CH} (800 and 1379 cm^{-1}) in the aromatic system of imidazolium and its framework vibration at 1458 cm^{-1} demonstrated the successful, noncovalent functionalization of f-RGO with [BMIM][BF₄].

XPS measurements were performed on the f-RGO and GO deposited on Si substrates to determine the f-RGO chemical

composition and elemental chemical state. Figure 4a and b shows the XPS survey spectra of GO and f-RGO, respectively. Because of the harsh oxidation conditions under the modified Hummers and Offeman method, abundant oxygen-containing functional groups, such as epoxide, hydroxyl, carbonyl, and carboxyl, were present at both the edges and defects of GO²¹ thus causing the O 1s peak to exhibit a large intensity. The XPS spectrum of f-RGO clearly exhibited a decrease in O 1s peak intensity and a corresponding increase in C 1s peak intensity indicating that significant deoxygenation took place during chemical reduction. In fact, complete reduction of GO is impossible. Moreover, an additional F 1s peak originating from the [BMIM][BF₄] anion and a N 1s peak appeared simultaneously in the XPS spectrum of f-RGO providing spectroscopic evidence of the noncovalent functionalization of RGO with [BMIM][BF₄]. No visible B peak was found in the f-RGO XPS spectrum because of the low atomic sensitivity of element B. Figure 4c shows the deconvoluted GO C 1s region revealing the presence of four types of carbon bonds: C-C (284.8 eV), C-O (286.9 eV), C=O (288.1 eV), and O-C=O (289.2 eV).³⁹ The high-resolution XPS spectrum in

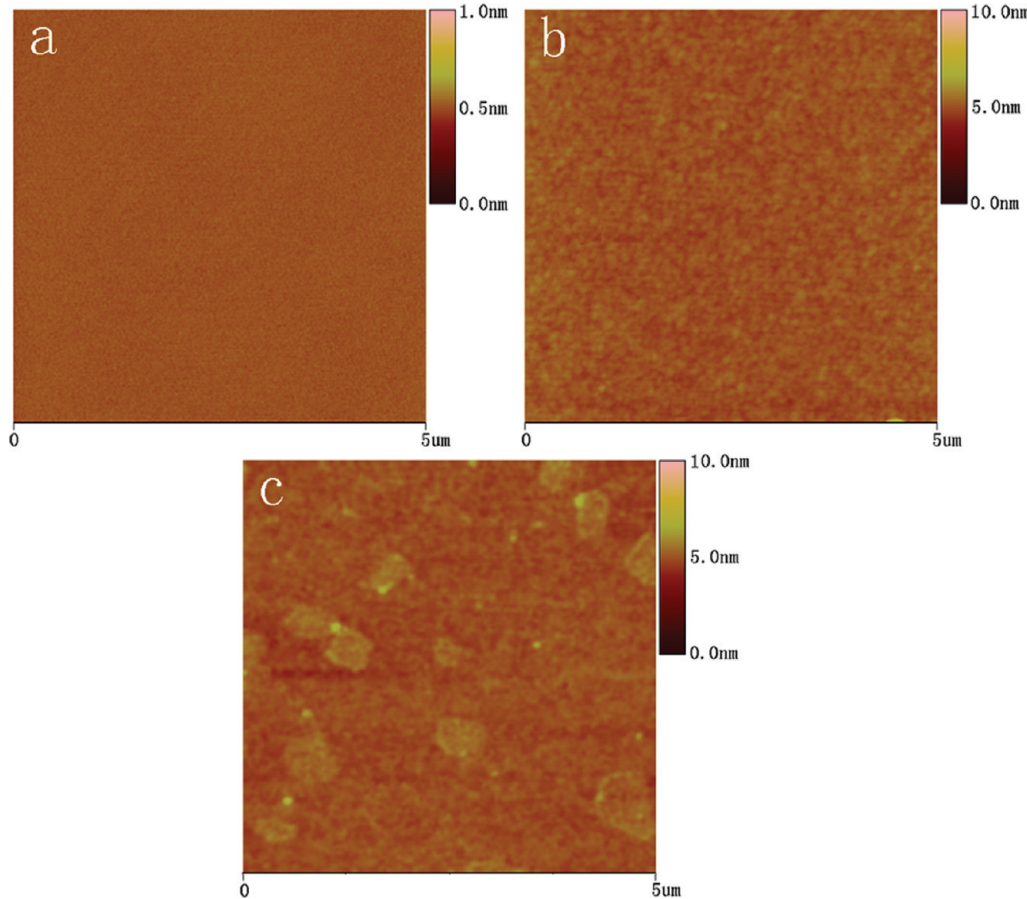


Figure 5. Tapping-mode AFM images of (a) hydroxylated Si, (b) pure ILs film, and (c) (0.1)f-RGO/ILs nanocomposite film on Si substrates.

Figure 4d shows that the intensity of the C–C peak became predominant after GO was reduced to f-RGO in the presence of [BMIM][BF₄], whereas the intensities of all the peaks related to the oxidized carbon species, especially the C–O peak, were greatly weakened indicating that these oxygen-containing functional groups were mostly removed from GO after chemical reduction. Aside from the original species, an additional component was seen at 286.2 eV corresponding to a carbon bound to a nitrogen (C–N) because of both the noncovalent functionalization of RGO with [BMIM][BF₄] and the chemical reduction with hydrazine.⁴⁰ Figure 4e shows the deconvoluted f-RGO N 1s region. The single strong peak at 401.8 eV was attributed to N atoms from the [BMIM][BF₄] imidazolium ring again confirming that the RGO was effectively functionalized by [BMIM][BF₄]. The weak shoulder at 399.7 eV corresponded to trace N atoms incorporated into the RGO during chemical reduction with hydrazine.⁴⁰

AFM was used to directly observe the structures of the hydroxylated Si surface, the pure IL film, and the (0.1)f-RGO/IL film coated onto a Si surface. Compared with the smooth hydroxylated Si surface shown in Figure 5a, both Figure 5b and c showed densely packed films on the Si surface. The (0.1)f-RGO/IL film in Figure 5c shows visible f-RGO in the nanocomposite films, which were seen as submicroisolated islands rather than as a homogeneous monolayer. As well, the film had a flat but fuzzy surface morphology because of the coverage of [BMIM][PF₆].

XPS analysis was repeated on all as-prepared films to affirm the formation of nanocomposite films on Si substrates. Figure 6

shows the stacked XPS survey spectra of the three nanocomposite films and the pure IL film. The stacked high-resolution XPS spectra of P 2p are also presented in Figure 6c in view of the weak intensity of the P 2p peak in the survey spectra. As shown in Figure 6a, an increase in the F 1s peaks of the films was observed compared with that of f-RGO (Figure 4b) resulting from the presence of the dominant [BMIM][PF₆]. The increase in O 1s peaks observed may have resulted from the adsorbed water molecules in the IL-based nanocomposite films. Furthermore, the intensities of the F 1s and P 2p peaks gradually decreased in the order of the pure ILs > (0.2)f/RGO-ILs > (0.1)f-RGO/ILs > (0.01)f-RGO/ILs indicating that the relative [BMIM][PF₆] content in these films decreased. Meanwhile, the C 1s peak at 284.8 eV, shown in Figure 6b, became asymmetric and gradually broadened toward the high-binding energy side in the same sequence accompanied by the increase in f-RGO with residual oxygen-containing functional groups in the nanocomposite films. These XPS results confirm that the three kinds of nanocomposite films and the pure IL film were successfully formed on the Si substrates.

The adhesion behavior between the microsphere of the colloidal probe and the sample surfaces is shown in Figure 7. All the nanocomposite and pure IL film exhibited relatively low adhesive forces, whereas the superhydrophilic hydroxylated Si surface showed strong adhesion because of the large capillary force caused by the adsorbed water, which could also have been reflected by their static water contact angles (Table 1), that is, surface wettability. A tendency toward reduced adhesive force

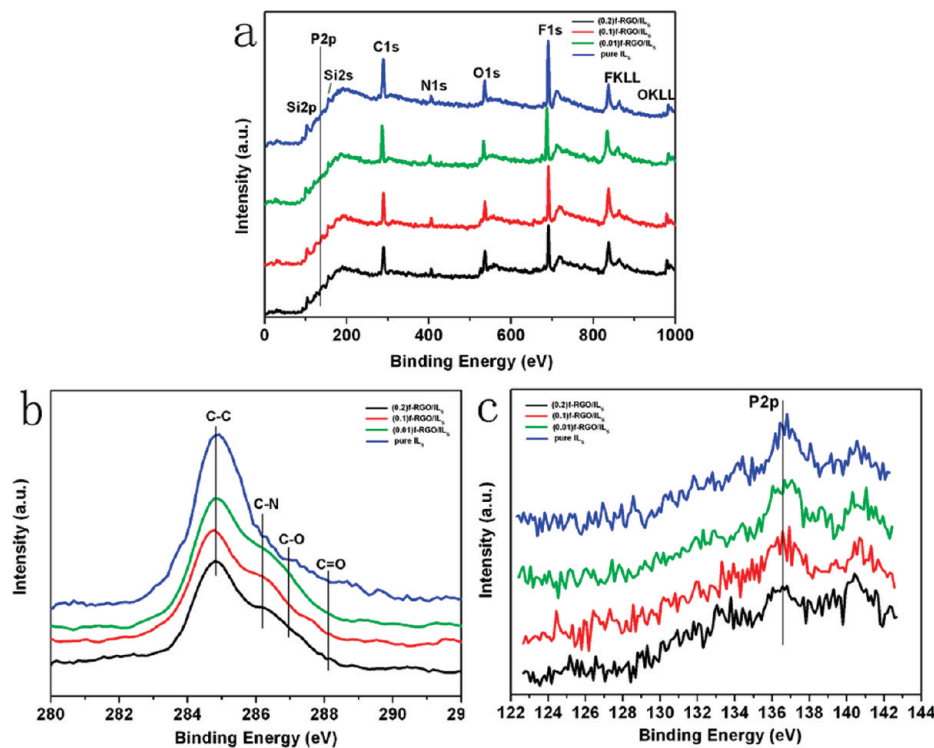


Figure 6. (a) Stacked XPS survey spectra, (b) stacked C 1s XPS spectra, and (c) stacked P 2p XPS spectra of various films.

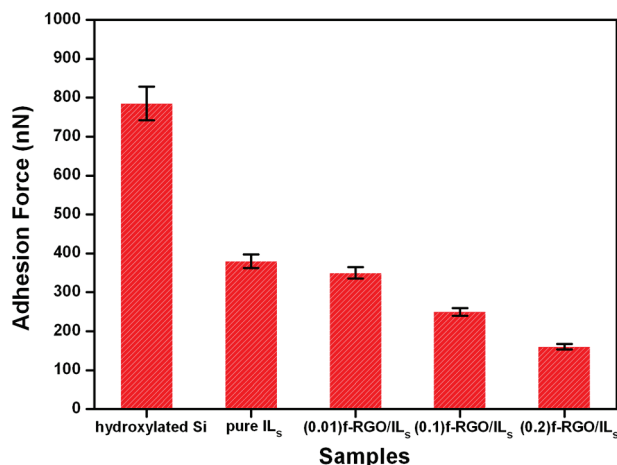


Figure 7. Adhesive forces between the microsphere of the colloid probe and the surfaces of various films.

Table 1. Static Water Contact Angles (deg)

hydroxylated Si	pure IL _s	(0.01)f-RGO/IL _s	(0.1)f-RGO/IL _s	(0.2)f-RGO/IL _s
<5	52	55	61	74

with increased f-RGO content in nanocomposite films was also observed. Adhesion between contact interfaces is produced under the combined action of van der Waals, capillary, electrostatic, and chemical bonding on the micro/nanoscale.⁴¹ When a liquid film is introduced at the contact interface either through adsorption or by deposition, the adhesive force is mainly dominated by the capillary force resulting from film condensation and

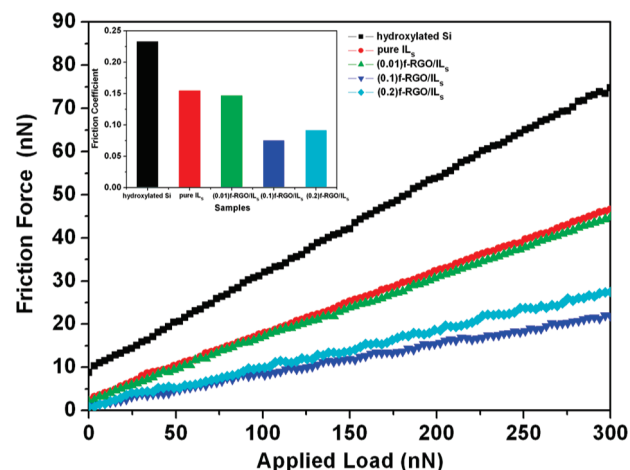


Figure 8. (a) Nanofriction force versus load curves of various films. The inset is nanofriction coefficients (NFC) directly derived from slope of the curves.

the adsorbed water.^{41,42} Thus, a decrease in the capillary force in nanocomposite films, caused by decreasing IL components and increasing graphene component, could be a major reason for the low adhesive force observed in the films.

The nanotribological performances of these samples with linearly increased loads are shown in Figure 8. The linear relationship of the friction force versus the external load can be described by a modified form of Amonton's law⁴³ in which the lateral force (F_L) is given by $F_L = \mu F_N + F_0$, where μ is the nanofriction coefficient (NFC), F_N is the normal load, and F_0 is the friction force when the external load is zero. The slope of the curve can be used as the friction coefficient and is summarized in

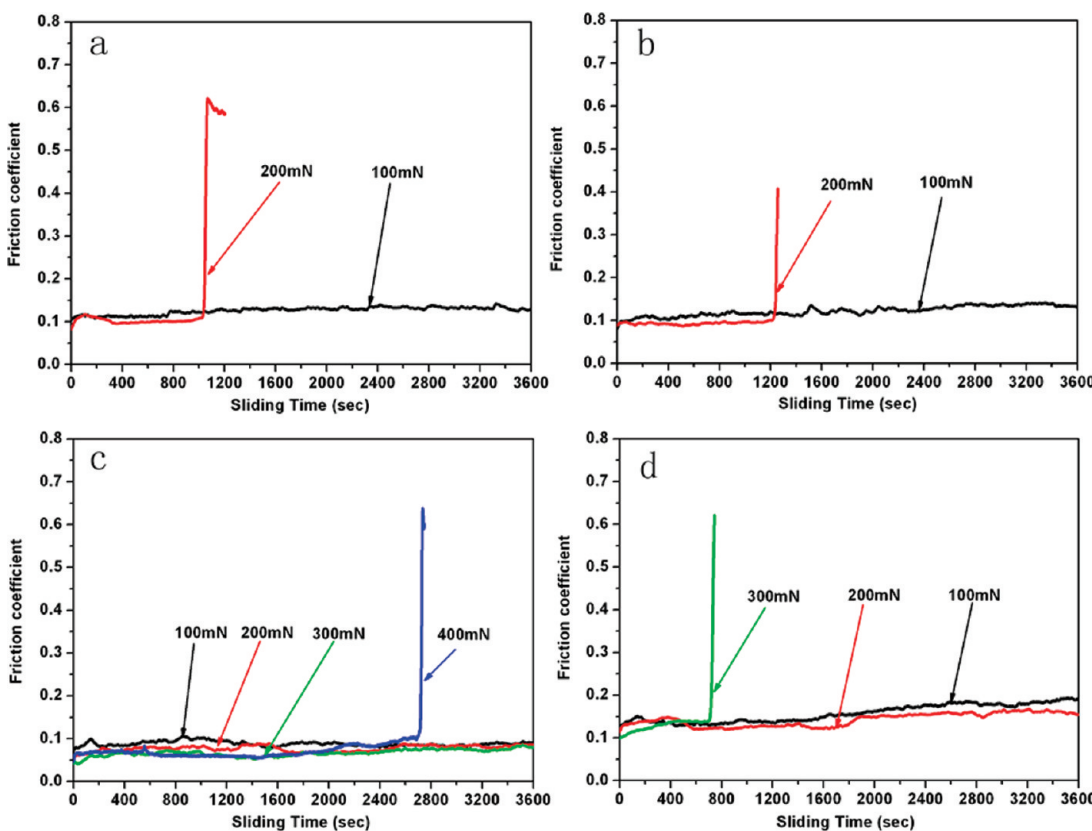


Figure 9. Variation in microfriction coefficient with sliding time for various films at sliding frequency of 2 Hz: (a) pure ILs; (b) (0.01)f-RGO/ILs; (c) (0.1)f-RGO/ILs; (d) (0.2)f-RGO/ILs.

the inset of Figure 8. The nanofriction forces of these samples changed roughly in the order of their adhesive forces with the exception of (0.1)f-RGO/ILs. This is easy to understand because the adhesive force has an effect on nanotribological properties. Several studies have shown that nanofriction decreases with the reduction in adhesion. The hydroxylated Si surface showed a maximum NFC of 0.23 among all the tested samples because the capillary effect caused by the adsorbed water produced high friction resistance on the surface, whereas the pure IL film exhibited a lower NFC of 0.15 because of its low adhesion and excellent nanolubricating property. Compared with the pure IL film, the more hydrophobic (0.1)f-RGO/ILs showed a minimum NFC of 0.07. The improved nanolubricity was attributed to the appropriate [BMIM][PF₆] amount on and among the f-RGO, which facilitated microsphere sliding because of the low shear strength in the system. Here, capillary effects were not easy to produce.⁴⁴ In addition, the presence of the few-layer graphene and better nanofriction property compared with the Si surface also contributed to the low NFC. As for (0.2)f-RGO/ILs, an enhanced NFC of 0.09 was observed; it is believed that many of the graphene nanosheets overlapped adjacent graphene nanosheets on the substrate surface along the edges during formation of nanocomposite film from the dispersion of high f-RGO density. The increased surface roughness resulted in great energy dissipation and degraded the (0.2)f-RGO/ILs' nanofriction performance. In short, uniformly distributed, nonoverlapping f-RGO in the plane further reduced the nanofriction of IL thin films, which are already being treated as promising friction-reducing and antiwear coatings.

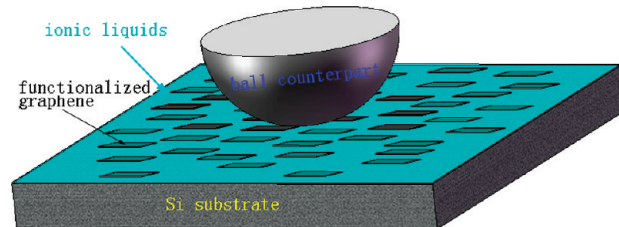


Figure 10. Schematic illustration of microfriction mechanism of nanocomposite films.

The microtribological performances of these thin films are very important for their application in protection layers. As shown in Figure 9a, the pure IL film exhibited limited load-carrying capacity characterized by a short antiwear life of 1028 s under relatively mild conditions (applied load of 200 mN, sliding frequency of 2 Hz). This may be because ILs are easily worn out and are not strong enough to prevent the direct contact between asperities on the steel ball counterpart and the Si surfaces under a relatively high applied load. For (0.01)f-RGO/ILs with a relatively low graphene content, a load-carrying capacity and micro-friction coefficient (MFC) parallel to those of the pure IL film were observed (Figure 9b). (0.1)f-RGO/ILs (Figure 9c) exhibited both reduced MFCs below 0.1 under all applied loads and a lengthened antiwear life of over 1 h under an applied load of 200 mN, which did not fail within 1 h until 400 mN. The greatly enhanced load-carrying capacity and lubricating property may be attributed to the synergistic effect of the immobilizing f-RGO component as the load-carrying phase and the mobile [BMIM][PF₆] component as the

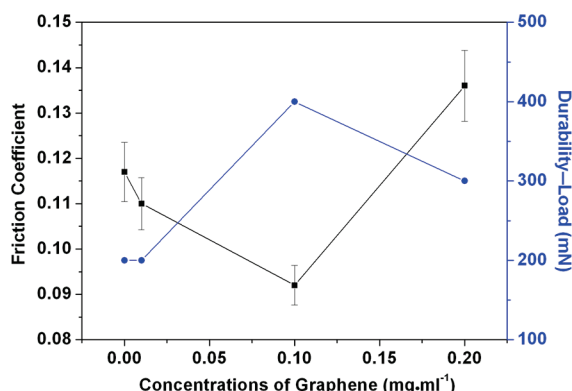


Figure 11. Friction coefficient under 100 mN and durability load as a function of the density of f-RGO in acetone dispersion of graphene–IL.

lubrication phase. As schematized in Figure 10, the more compliant few-layer graphene could adhere to the Si surface under the applied load remaining localized over the same contact area. Consequently, the antiwear graphene layer produced, which showed high flexibility and mechanical stiffness under applied loads, prevented the direct contact between asperities on the steel ball counterpart and the Si surfaces and absorbed the energy generated by compression and shear during friction sliding.⁹ A possible explanation for the reduction in MFC may be that graphene interlayer sliding decreased the friction; this agrees well with previously reported results.⁹ Furthermore, the presence of immobilizing f-RGO makes it difficult to peel off the [BMIM][PF₆] embedded among them during friction sliding. Meanwhile, the [BMIM][PF₆] adsorbed on f-RGO reorganized themselves into the original state after being mechanically disrupted during sliding, which is a self-replenishing property, thereby maintaining their good lubricating property. However, when the density of f-RGO further increased in the dispersion of the functionalized graphene–ILs, the load-carrying capacity of the formed (0.2)f-RGO/ILs (Figure 9d) started to decrease; increased and fluctuating MFCs greater than 0.1 under all applied loads were also given. The degradation of microtribological performances could be explained by the partial edge-overlapping of individual graphene adsorption on the surface. In other words, the overlapping adsorption of redundant f-RGO lowered the [BMIM][PF₆] lubricating component and increased surface roughness causing a high and unstable MFC. Because of the lower [BMIM][PF₆] component, overlapping f-RGO were seldom restricted by [BMIM][PF₆] and were easily peeled off during friction sliding resulting in low antiwear capacity.

Figure 11 shows both MFCs of these films under an applied load of 100 mN and their durability load as a function of f-RGO density in the dispersion of functionalized graphene–ILs. As analyzed above, either a remarkable increase in the durability load or a reduction in MFC with the increase of the density of f-RGO occurred; however, when the f-RGO density continued to rise, most of the individual graphene sheets overlapped on the substrate surface resulting in a decrease in the microtribological property of the nanocomposite films. Therefore, only an appropriate amount of graphene uniformly distributed on the substrate surface without overlapping may give the best micro/nanotribological behaviors of the nanocomposite films. These experimental observations shed light on designing graphene–IL nanocomposite films with excellent comprehensive tribological properties.

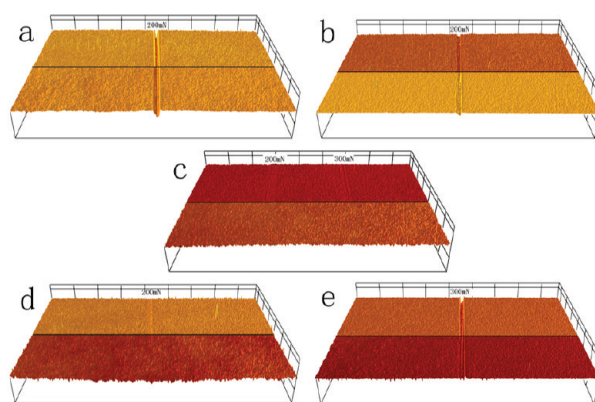


Figure 12. 3-D profile images of the friction surfaces of (a) pure IL film under applied load of 200 mN at failure, (b) (0.01)f-RGO/ILs film under applied load of 200 mN at failure, (c) (0.1)f-RGO/ILs film under applied loads of 200 mN and 300 mN for 1 h, (d) (0.2)f-RGO/ILs under applied load of 200 mN for 1 h and applied load of 300 mN at failure. All experiments were carried out at sliding frequency of 2 Hz.

Images of the worn film surfaces are shown in Figure 12 to further compare their antiwear properties; the lower half of each image gives a Si surface that has undergone ultrasonic cleaning to remove the lubrication films. As shown in Figure 12a, a very deep wear scar appeared on the Si surface with the pure IL film when it failed under an applied load of 200 mN; the same is true for (0.01)f-RGO/ILs (Figure 12b). The Si surface of (0.2)f-RGO/ILs showed no visible wear scar under an applied load of 200 mN after sliding for 1 h as shown in Figure 9d. However, when the applied load rose to 300 mN, Figure 12e shows a slight wear, whereas the Si surface with the (0.1)f-RGO/ILs (Figure 12c) showed no wear scar under applied loads of both 200 and 300 mN. These results further confirm that (0.1)f-RGO/ILs could provide good wear protection.

CONCLUSIONS

The stable dispersion of graphene nanosheets in aqueous and acetone solutions was successfully achieved with the aid of freely soluble [BMIM][BF₄] ILs. A new noncovalently functionalized graphene–IL nanocomposite lubrication film was also formed on the Si substrate by combining [BMIM][BF₄]-stabilized graphene nanosheets with the excellent mechanical properties and better lubrication performance of the [BMIM][PF₆] IL. In addition, the effect of the density of functionalized graphene in the functionalized graphene–IL dispersion on micro/nanotribological performances of the resulting nanocomposite film was explored. Nanocomposite films with the appropriate amount of functionalized graphene uniformly distributed on the substrate surface without overlapping provided higher load-carrying capacity and lower micro/nanofriction resistance compared with the pure [BMIM][PF₆] film. This is attributed to the synergic effect between the load-carrying graphene and the lubricating ILs. The present study suggests that the functionalized graphene–IL nanocomposite lubrication film expands the scope of IL-based lubrication film and thus has great potential in MEMS/NEMS applications.

AUTHOR INFORMATION

Corresponding Author

*Phone: 86-931-4968080. Fax: 86-931-8277088. E-mail: lpwang@licp.ac.cn.

■ ACKNOWLEDGMENT

The authors are grateful to the financial support from Natural Science Foundation of China (Grant No. 50823008) and National 973 Program (Grant No. 2011CB706603).

■ REFERENCES

- (1) (a) Booth, T. J.; Blake, P.; Rahul, R. N.; Jiang, D.; Hill, E. W.; Bangert, U.; Bleloch, A.; Gass, M.; Novoselov, K. S.; Katsnelson, M. I.; Geim, A. K. *Nano Lett.* **2008**, *8*, 2442. (b) Lee, C. E.; Wei, X.; Kysar, J. W.; Hone, J. *Science* **2008**, *321*, 385.
- (2) (a) Balandin, A. A.; Ghosh, S.; Bao, W. Z.; Calizo, I.; Teweldebrhan, D.; Miao, F.; Lau, C. N. *Nano Lett.* **2008**, *8*, 902. (b) Su, C. Y.; Xu, Y. P.; Zhang, W. J.; Zhao, J. W.; Tang, X. H.; Tsai, C. H.; Li, L. *J. Chem. Mater.* **2009**, *21*, 5674.
- (3) (a) Geim, A. K.; Novoselov, K. S. *Nat. Mater.* **2007**, *6*, 183. (b) Katneson, M. I. *Mater. Today* **2007**, *10*, 20.
- (4) Areshkin, D. A.; White, C. T. *Nano Lett.* **2007**, *7*, 3253.
- (5) (a) Lu, C. H.; Yang, H. H.; Zhu, C. L.; Chen, X.; Chen, G. N. *Angew. Chem., Int. Ed.* **2009**, *48*, 4785. (b) Schedin, F.; Geim, A. K.; Morozov, S. V.; Hill, E. W.; Blake, P.; Katsnelson, M. I.; Novoselov, K. S. *Nat. Mater.* **2007**, *6*, 652.
- (6) (a) Pasricha, R.; Gupta, S.; Srivastava, A. K. *Small* **2009**, *5*, 2253. (b) Vickery, J. L.; Patil, A. J.; Mann, S. *Adv. Mater.* **2009**, *21*, 2180. (c) Stankovich, S.; Dikin, D. A.; Dommett, G. H. B.; Kohlhaas, K. M.; Zimney, E. J.; Stach, E. A.; Piner, R. D.; Nguyen, S. T.; Ruoff, R. S. *Nature* **2006**, *442*, 282.
- (7) Yoo, E. J.; Kim, J.; Hosono, E.; Zhou, H. S.; Kudom, T.; Honma, I. *Nano Lett.* **2008**, *8*, 2277.
- (8) Stoller, M. D.; Park, S.; Zhu, Y.; An, J.; Ruoff, R. S. *Nano Lett.* **2008**, *8*, 3498.
- (9) (a) Lee, C. G.; Wei, X. D.; Li, Q. Y.; Carpick, R.; Kysar, J. W.; Hone, J. *Phys. Status Solidi B* **2009**, *246*, 2562. (b) Bonelli, F.; Manini, N.; Cadelano, E.; Colombo, L. *Eur. Phys. J. B* **2009**, *70*, 449. (c) Filletter, T.; Bennewitz, R. *Phys. Rev. B* **2010**, *81*, 155412. (d) Lee, C. G.; Li, Q. Y.; Kalb, W.; Liu, X. Z.; Berger, H.; Carpick, R. W.; Hone, J. *Science* **2010**, *328*, 76.
- (10) Filletter, T.; McChesney, J. L.; Bostwick, A.; Rotenberg, E.; Emtsev, K. V.; Seyller, T.; Horn, K.; Bennewitz, R. *Phys. Rev. Lett.* **2009**, *102*, 086102.
- (11) Lee, H.; Lee, N.; Seo, Y.; Eom, J.; Lee, S. *Nanotechnology* **2009**, *20*, 325701.
- (12) Ou, J. F.; Wang, J. Q.; Liu, S.; Mu, B.; Ren, J. F.; Wang, H. G.; Yang, S. R. *Langmuir* **2010**, *26*, 15830.
- (13) Wilkes, J. S. *Green Chem.* **2002**, *4*, 73.
- (14) Earle, M. J.; Esperanca, J.; Gilea, M. A.; Lopes, J. N. C.; Rebelo, L. P. N.; Magee, J. W.; Seddon, K. R.; Widegren, J. A. *Nature* **2006**, *439*, 831.
- (15) (a) Seddon, K. R. *Nat. Mater.* **2003**, *2*, 363. (b) Rogers, R. D.; Seddon, K. R. *Science* **2003**, *302*, 792. (c) Plechkova, N. V.; Seddon, K. R. *Chem. Soc. Rev.* **2008**, *37*, 123.
- (16) Zhou, F.; Liang, Y. M.; Liu, W. M. *Chem. Soc. Rev.* **2009**, *38*, 2590.
- (17) (a) Ye, C. F.; Liu, W. M.; Chen, Y. X.; Yu, L. G. *Chem. Commun.* **2001**, *1*, 2244. (b) Yao, M. H.; Liang, Y. M.; Xia, Y. Q.; Zhou, F. *ACS Appl. Mater. Interfaces* **2009**, *1*, 467. (c) Phillips, B. S.; Zabinski, J. S. *Tribol. Lett.* **2004**, *17*, 533. (d) Jin, C. M.; Ye, C. F.; Phillips, B. S.; Zabinski, J. S.; Liu, X. Q.; Liu, W. M.; Shreeve, J. M. *J. Mater. Chem.* **2006**, *16*, 1529.
- (18) (a) Zhao, W. J.; Mo, Y. F.; Pu, J. B.; Bai, M. W. *Tribol. Int.* **2009**, *42*, 828. (b) Palacio, M.; Bhushan, B. *Adv. Mater.* **2008**, *20*, 1194. (c) Nainaparampil, J. J.; Phillips, B. S.; Eapen, K. C.; Zabinski, J. S. *Nanotechnology* **2005**, *16*, 2474.
- (19) (a) Bhushan, B.; Palacio, M.; Kinzig, B. *J. Colloid Interface Sci.* **2008**, *317*, 275. (b) Zhao, W. J.; Wang, Y.; Wang, L. P.; Bai, M. W.; Xue, Q. J. *Colloids Surf., A* **2010**, *361*, 118. (c) Pu, J. B.; Wang, L. P.; Mo, Y. F.; Xue, Q. J. *J. Colloid Interface Sci.* **2011**, *354*, 858.
- (20) Novoselov, K. S.; Geim, A. K.; Morozov, S. V.; Jiang, D.; Zhang, Y.; Dubonos, S. V.; Grigorieva, I. V.; Firsov, A. A. *Science* **2004**, *306*, 666.
- (21) (a) Hernandez, Y.; Nicolosi, V.; Lotya, M.; Blighe, F. M.; Sun, Z. Y.; De, S.; McGovern, I. T.; Holland, B.; Byrne, M.; Gun'ko, Y. K.; et al. *Nat. Nanotechnol.* **2008**, *3*, 563. (b) Stankovich, S.; Dikin, D. A.; Piner, R. D.; Kohlhaas, K. A.; Kleinhammes, A.; Jia, Y.; Wu, Y.; Nguyen, S. T.; Ruoff, R. S. *Carbon* **2007**, *45*, 1558.
- (22) Schniepp, H. C.; Li, J. L.; McAllister, M. J.; Sai, H.; Herrera-Alonso, M.; Adamson, D. H.; Prud'homme, R. K.; Car, R.; Saville, D. A.; Aksay, I. A. *J. Phys. Chem. B* **2006**, *110*, 8535.
- (23) (a) Dato, A.; Radmilovic, V.; Lee, Z. H.; Phillips, J.; Frenklach, M. *Nano Lett.* **2008**, *8*, 2012. (b) Reina, A.; Jia, X.; Ho, J.; Nezich, D.; Son, H.; Bulovic, V.; Dresselhaus, M. S.; Kong, J. *Nano Lett.* **2009**, *9*, 30.
- (24) Park, S.; Ruoff, R. S. *Nat. Nanotechnol.* **2010**, *5*, 309.
- (25) Si, Y.; Samulski, E. T. *Nano Lett.* **2008**, *8*, 1679.
- (26) (a) Li, D.; Muller, M. B.; Gilje, S.; Kaner, R. B.; Wallace, G. G. *Nat. Nanotechnol.* **2008**, *3*, 101. (b) Wang, G. X.; Shen, X. P.; Wang, B.; Yao, J.; Park, J. *Carbon* **2009**, *47*, 1359. (c) Bai, H.; Xu, Y. X.; Zhao, L.; Li, C.; Shi, G. Q. *Chem. Commun.* **2009**, 1667. (d) Liu, H.; Gao, J.; Xue, M. Q.; Zhu, N.; Zhang, M. N.; Cao, T. B. *Langmuir* **2009**, *25*, 12006. (e) Li, F. H.; Bao, Y.; Chai, J.; Zhang, Q. X.; Han, D. X.; Niu, L. *Langmuir* **2010**, *26*, 12314.
- (27) (a) Yang, H. F.; Shan, C. S.; Li, F. H.; Han, D. X.; Zhang, Q. X.; Niu, L. *Chem. Commun.* **2009**, 3880. (b) Zhang, B. Q.; Ning, W.; Zhang, J. M.; Qiao, X.; Zhnag, J.; He, J. S.; Liu, C. Y. *J. Mater. Chem.* **2010**, *20*, 5401. (c) Zhou, X. S.; Wu, T. B.; Ding, K. L.; Hu, B. J.; Hou, M. Q.; Han, B. X. *Chem. Commun.* **2010**, *46*, 386. (d) Liu, N.; Luo, F.; Hou, H. X.; Liu, Y. H.; Zhang, C.; Chen, J. *Adv. Funct. Mater.* **2008**, *18*, 1518.
- (28) (a) Hummers, W. S.; Offeman, R. E. *J. Am. Chem. Soc.* **1958**, *80*, 1339. (b) Cote, L. J.; Kim, F.; Huang, J. *J. Am. Chem. Soc.* **2009**, *131*, 1043.
- (29) Vakarelski, I. U.; Brown, S. C.; Rabinovich, Y. I.; Moudgil, B. M. *Langmuir* **2004**, *20*, 1724.
- (30) Yang, S.; Zhang, H.; Hsu, S. M. *Langmuir* **2007**, *23*, 1195.
- (31) (a) Fukushima, T.; Kosaka, A.; Ishimura, Y.; Yamamoto, T.; Takigawa, T.; Ishii, N.; Aida, T. *Science* **2003**, *300*, 2072. (b) Shim, Y. S.; Kim, H. J. *ACS Nano* **2009**, *3*, 1693.
- (32) Güneş, F.; Shin, H. J.; Biswas, C.; Han, G. H.; Kim, E. S.; Chae, S. J.; Choi, J. Y.; Lee, Y. H. *ACS Nano* **2010**, *4*, 4595.
- (33) Li, N.; Wang, Z. Y.; Zhao, K. K.; Shi, Z. J.; Gu, Z. N.; Xu, S. K. *Carbon* **2010**, *48*, 255.
- (34) Nethravathi, C.; Nisha, T.; Ravishankar, N.; Shivakumara, C.; Rajamathi, M. *Carbon* **2009**, *47*, 2054.
- (35) Ferrari, A. C.; Meyer, J. C.; Scardaci, V.; Casiraghi, C.; Lazzari, M.; Mauri, F.; Piscanec, S.; Jiang, D.; Novoselov, K. S.; Roth, S.; et al. *Phys. Rev. Lett.* **2006**, *97*, 187401.
- (36) (a) Kudin, K. N.; Ozbas, B.; Schniepp, H. C.; Prud'homme, R. K.; Aksay, I. A.; Car, R. *Nano Lett.* **2008**, *8*, 36. (b) Graf, D.; Molitor, F.; Ensslin, K.; Stampfer, C.; Jungen, A.; Hierold, C.; Wirtz, L. *Nano Lett.* **2007**, *7*, 238. (c) Choi, E. Y.; Han, T. H.; Hong, J.; Kim, J. E.; Lee, S. H.; Kim, H. W.; Kim, S. O. *J. Mater. Chem.* **2010**, *20*, 1907.
- (37) Shen, J. F.; Hu, Y. Z.; Li, C.; Qin, C.; Shi, M.; Ye, M. X. *Langmuir* **2009**, *25*, 6122.
- (38) Kim, T. Y.; Lee, H. W.; Kim, J. E.; Suh, K. S. *ACS Nano* **2010**, *4*, 1612.
- (39) Xu, Y.; Bai, H.; Lu, G.; Li, C.; Shi, G. *J. Am. Chem. Soc.* **2008**, *130*, 5856.
- (40) Wang, Y.; Shao, Y. Y.; Matson, D. W.; Li, J. H.; Lin, Y. H. *ACS Nano* **2010**, *4*, 1790.
- (41) Kim, S. H.; Asay, D. B.; Dugger, M. T. *Nano Today* **2007**, *2*, 22.
- (42) Liu, H. W.; Bhushan, B. *Ultramicroscopy* **2002**, *91*, 185.
- (43) (a) Brewer, N. J.; Beaker, B. D.; Leggett, G. J. *Langmuir* **2001**, *17*, 1970. (b) Foster, T. T.; Alexander, M. R.; Leggett, G. J.; McAlpine, E. *Langmuir* **2006**, *22*, 9254.
- (44) Bhushan, B.; Palacio, M.; Kinzig, B. *J. Colloid Interface Sci.* **2008**, *317*, 275.